

Use of plasma treatment to grow carbon nanotube forests on TiN substrate

S. Esconjauregui, B. C. Bayer, M. Fouquet, C. T. Wirth, F. Yan et al.

Citation: *J. Appl. Phys.* **109**, 114312 (2011); doi: 10.1063/1.3587234

View online: <http://dx.doi.org/10.1063/1.3587234>

View Table of Contents: <http://jap.aip.org/resource/1/JAPIAU/v109/i11>

Published by the [American Institute of Physics](#).

Related Articles

Influence of the embedding matrix on optical properties of Ge nanocrystals-based nanocomposite

J. Appl. Phys. **113**, 053512 (2013)

Fabrication of Bi₂Te₃ nanowire arrays and thermal conductivity measurement by 3 ω -scanning thermal microscopy

J. Appl. Phys. **113**, 054308 (2013)

Controlled route to the fabrication of carbon and boron nitride nanoscrolls: A molecular dynamics investigation

J. Appl. Phys. **113**, 054306 (2013)

Electrodynamic control of the nanofiber alignment during electrospinning

Appl. Phys. Lett. **102**, 053111 (2013)

Evaluation of field emission parameters in a copper nano-tip based diode

J. Appl. Phys. **113**, 053303 (2013)

Additional information on *J. Appl. Phys.*

Journal Homepage: <http://jap.aip.org/>

Journal Information: http://jap.aip.org/about/about_the_journal

Top downloads: http://jap.aip.org/features/most_downloaded

Information for Authors: <http://jap.aip.org/authors>

ADVERTISEMENT



AIPAdvances

Now Indexed in
Thomson Reuters
Databases

Explore AIP's open access journal:

- Rapid publication
- Article-level metrics
- Post-publication rating and commenting

Use of plasma treatment to grow carbon nanotube forests on TiN substrate

S. Esconjauregui,^{1,a)} B. C. Bayer,¹ M. Fouquet,¹ C. T. Wirth,¹ F. Yan,¹ R. Xie,¹ C. Ducati,² C. Baetz,³ C. Castellarin-Cudia,^{4,5} S. Bhardwaj,⁵ C. Cepek,⁵ S. Hofmann,¹ and J. Robertson¹

¹Department of Engineering, University of Cambridge, Cambridge CB3 0FA, United Kingdom

²Department of Materials Science and Metallurgy, University of Cambridge, Cambridge CB2 3QZ, United Kingdom

³Institute of Ion Beam Physics and Materials Research, Forschungszentrum Dresden Rossendorf e.V., P.O. Box 51 01 19, D-01314 Dresden, Germany

⁴Sincrotrone Trieste SCpA, Strada Statale, 14 km 163.4, I-34149, Trieste, Italy

⁵Istituto Officina dei Materiali-CNR Laboratorio TASC, s.s. 14, km 163.4, I-34012 Trieste, Italy

(Received 1 December 2010; accepted 7 April 2011; published online 7 June 2011)

Hydrogen plasma pretreatment is used to enforce the growth of vertically-aligned carbon nanotube forests on TiN substrates. The evolution of the substrate, catalyst, and nanotubes are studied by *in situ* and ex-situ photoemission and X-ray diffraction in order to understand the growth mechanism. We find that TiN retains its crystallographic structure and its conductivity during plasma pretreatment and nanotube growth, which is confirmed by electrical measurements. Plasma pretreatment is found to favor the growth of nanotube forests by root growth, as it binds the catalyst nanoparticles more strongly to the substrate than thermal pretreatment. We find that plasma pretreatment time should be limited, otherwise poor or no growth is found. © 2011 American Institute of Physics. [doi:10.1063/1.3587234]

I. INTRODUCTION

Owing to their remarkable properties, carbon nanotubes (CNTs) are envisaged as the component materials of many technologies, such as interconnects in integrated circuits, field emitters, supercapacitor electrodes, sensors, and thermal management surfaces.^{1–6} Many of these applications require the nanotubes to be grown or placed directly on conducting substrates in the form of densely packed, small-diameter vertically aligned (VA) CNTs. This has led to intensive research, so that it is possible to grow CNTs efficiently, especially by chemical vapor deposition (CVD), in high purity, in bulk or on surfaces, and with a fairly clear understanding of the catalytic process and the influence of synthesis parameters.^{7–11} However, control of the growth of CNTs on metallic surfaces is more difficult and this can limit their use. In addition, for key applications, such as interconnects or field emitters, the synthesis conditions must allow the integration of nanotubes with existing materials and device structures.^{5,12} Therefore, further work on integration strategies is necessary to develop nanotube based devices.

The most direct process is to grow nanotubes directly on a substrate by CVD. Surface-growth CVD is, however, a complex catalytic process. The catalyst nanoparticles has two roles: (1) to decompose a carbon-containing source gas and (2) to act as nucleus for the nucleation and growth of nanotubes.^{13,14} The catalytic properties of the nanoparticles strongly depend on the catalyst-support interactions (CSIs) and these, in turn, influence the properties of the nucleated CNTs.¹⁵ Strong CSIs promote vertical alignment and favor root growth, and because the nanoparticles remain stable, bound to the support, nanotube diameter and surface density

are similar to those of the seeding nanoparticles. For these reasons, the growth of nanotube forests demands pretreatment and growth conditions that limit catalyst sintering and result in a suitable catalyst phase and topography, which, ideally, remain unchanged for the whole synthesis. This has been easily achieved on insulating supports, but it is more difficult on conductive materials.^{2,15–17} In general, metals substrate have a high surface energy, and they tend to interact strongly with the gas atmosphere or with the metal catalyst, obstructing its de-wetting. Hence, a metal-metal catalyst-support system, at the elevated temperatures and reactive atmospheres of CNT CVD, is hard to control.^{18–22} Indeed, there are only few reports of the growth of nanotube forests on metal supports such as Ta, TiN, or metal silicides.^{20–25}

We have recently demonstrated the effectiveness of hydrogen plasma pretreatment (PP) for growing nanotube forests on conductive TiN supports by thermal CVD.²³ Unlike purely thermal catalyst pretreatment (TP), which only gives limited or no growth, PP greatly facilitates the direct growth of high-density VA arrays of small-diameter nanotubes on TiN, with either Ni, Co, or Fe catalysts. Here, we investigate in detail the effects of plasma on nanoparticle formation and TiN stability. Our results show that the TiN support retains its crystallographic structure and conductivity during PP and CNT CVD, which is cross-checked with electrical characterization of nanotube forests. We further study TiN-Fe interactions and thus confirm that PP films result into more static nanoparticles than those obtained by TP. We finally suggest a nanotube growth model for PP nanoparticles. These findings are useful for understanding plasma action on nanoparticle formation/nanotube growth and represent a step further into nanotube integration.

^{a)}Electronic mail: cse28@cam.ac.uk.

II. EXPERIMENTAL METHODS

A. Catalyst preparation and nanotube growth

We use as substrate Si(100) coated with 200 nm of thermal SiO₂, on which we dc magnetron sputter 100 nm TiN. We then evaporate a nominally 0.5 or 1 nm thick layer of high-purity Ni, Co, or Fe, after exposing the TiN layer to air. Subsequently, the layers are subject to PP using a cold-wall plasma chamber (base pressure $\sim 10^{-6}$ mbar). PP is performed for 5 min at 450 to 800 °C in 100 mbar of H₂ and 50 W dc plasma. Note that H plasma is struck before starting to heat the chamber, as to assure that any temperature-driven process take place under plasma effect. Immediately after PP, the chamber is evacuated and CNT growth is carried out by purely thermal CVD in undiluted C₂H₂ at ~ 0.5 mbar for 10 min. The growth is terminated by evacuating the chamber up to a pressure of $\sim 10^{-3}$ mbar, which is maintained during cooling until reaching room temperature (RT).

B. Catalyst and nanotube characterization

TiN support, catalyst, and CNT films are examined by a field emission gun scanning electron microscope (FEG-SEM), high-resolution transmission electron microscope (HRTEM), and atomic force microscope (AFM) in tapping mode. Nanoparticle densities and sizes and nanotube diameters are estimated from SEM and HRTEM images using IMAGEJ and GWYDDION software. *Ex situ* structural analysis of the films is done by X-ray diffraction (XRD) in a Bruker axS D8 advance diffractometer (Cu-K _{α} X-ray source: 1.541 Å). Samples are placed with an off-angle of 16° to minimize interference from the sample holder. Measurements are taken at 40 kV/40 mA with the sample rotating in plane in Bragg-Brentano Theta-Theta geometry. Since samples are exposed to ambient prior to analysis, we consider oxidation effects when interpreting results.

C. XPS characterization

In situ and *ex situ* chemical state of surface samples is analyzed by X-ray photoelectron spectroscopy (XPS). All spectra are acquired at RT in normal emission geometry using a conventional Mg X-ray source ($h\nu = 1253.6$ eV), a 150° spherical sector electron energy analyzer, with an overall energy resolution of 1.2 eV. For data analysis, the photoelectron binding energy is referenced to the Fermi edge and/or by fixing the C 1s XPS binding energy (BE), due to hydrocarbon contamination, to 284.6 eV. The spectra are normalized to the incident photon flux and have been analyzed by performing a nonlinear mean square fit of the data following the Levenberg-Marquardt algorithm. We use a Shirley background and reproduce the photoemission intensity by using asymmetric Doniach-Sunjić functions convolved with Gaussian profiles. For calibration of Fe thickness, Fe is deposited *in situ* (in the same XPS chamber) at RT and a constant deposition rate of ~ 0.341 Å min⁻¹.

D. *In situ* XRD characterization

The samples are loaded in a semispherical Be chamber that allows passage/scattering of the X-rays in different geometries. They are first pretreated up to a temperature of 650 °C in 200 mbar of Ar:H₂ (30:10 sccm) for 30 min. Immediately after pretreatment, a gas flow of 1 sccm of C₂H₂ for another 30 min is added, keeping other conditions constant. After growth, samples are cooled down inside the chamber at a pressure of 10^{-5} mbar. *In situ* grazing incidence XRD is performed with a monochromatic X-ray beam of 11.5 keV and a wavelength of 1.07812 Å during each processing step (loading, pretreatment, and growth). These scans are recalculated to 1.541 Å for comparison with *ex situ* XRD. When interpreting results, we consider oxidation effects taking place during processing since Ar:H₂ gases are oxygen contaminated. For phase identification we use Powder Diffraction Files, International Centre for Diffraction Data, PCPDFWIN, version 2.4, 2003. JCPDS-ICDD, International Centre for Diffraction Data: Newtown Square, PA, USA, TiN: 38-1420, rutile TiO₂: 76-0326, and graphite: 65-6212.

E. Electrical characterization

Current-voltage (I-V) measurements are performed on bare TiN and on nanotube forests grown on TiN. For the latter characterization, we have first partially masked ($\sim 2 \times \sim 1$ cm²) TiN samples during Fe deposition. Then, the samples are subject to PP followed by CNT CVD at 600 °C; the other conditions are identical to those previously described in 2.1. To acquire I-V data, we use a two terminal Cascade Probe station set with a low bias condition ($|V| < 0.05$ V) during all measurements (as to avoid heating effects). The total resistance of the samples is determined from the slopes of a least squares fit to I-V response.

III. RESULTS AND DISCUSSION

Figure 1 summarizes PP results for CNT growth and nanoparticle formation. Cross-section SEM analysis shows how PP TiN-Fe systems lead to the nucleation and growth of nanotube forests (Fig. 1(a)). The surface density of these forests is $\sim 10^{12}$ CNTs cm⁻² and very homogeneous across the sample. The surface present cracks due to nanotube collapse by van der Waals forces, typical of forests with these densities [Fig. 1(a) inset].²⁶ HRTEM analysis shows no nanoparticles at the tip of the tubes, suggesting base growth [Fig. 1(b)]. The nanotubes are mainly double- and triple-walled, with diameters 5 ± 0.8 nm. We achieve similar growth using TiN-Ni or TiN-Co systems, down to a growth temperature of 480 °C [Fig. 1(c)]. The tube diameter using TiN-Co is similar to that obtained by using TiN-Fe [Fig. 1(c) inset]. All the forests nucleate from PP nanoparticles characterized by a high number density, very homogeneous sizes, and minimal separation or overlap [Figs. 1(d)–1(f)]. AFM analysis shows a smooth surface topology for all samples (not shown here). The 1 nm Fe, PP annealed at 600 °C for 5 min, shows a root-mean-square (RMS) of 3 nm and a nanoparticle height of ~ 5 nm with a lateral size distribution of 9 ± 1 nm. The

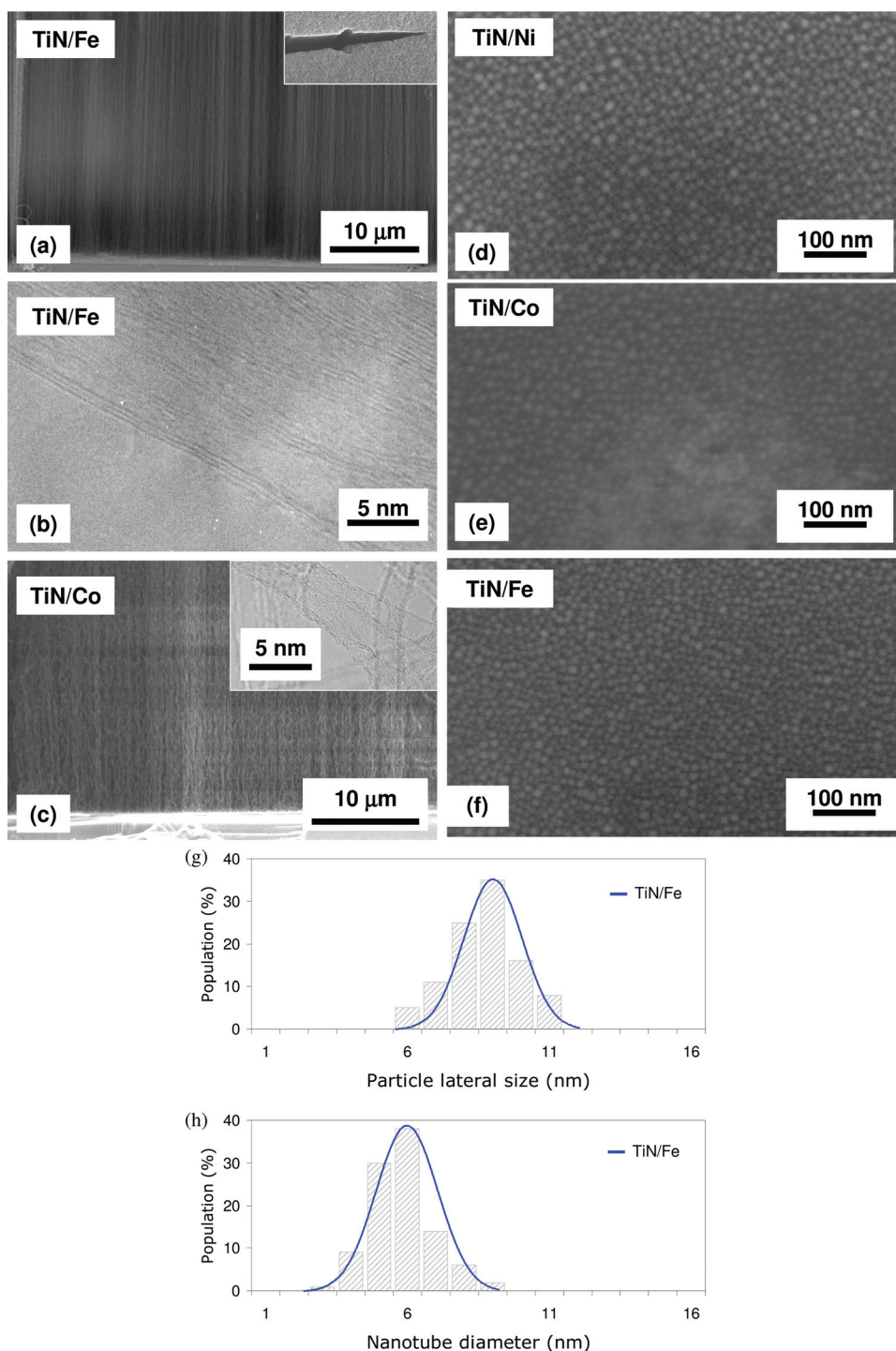


FIG. 1. (Color online) PP results for CNT growth and nanoparticle formation. Cross-section SEM images of CNTs grown for 10 min in 0.5 mbar of C_2H_2 on previously plasma pretreated (a) TiN/Fe and (c) TiN/Co films; the growth temperatures are 600 °C and 480 °C, respectively; (b) is a HRTEM image of CNTs grown in (a). (d) to (f) are respectively top-view SEM images of 1 nm Ni, Co, and Fe deposited onto TiN after PP for 5 min at 600 °C in 100 mbar of H_2 and dc plasma power of 50 W. (g) and (h) are histograms respectively showing lateral size distribution and diameter with Gaussian fitting (blue solid lines) of nanoparticles and nanotubes obtained using PP TiN/Fe system.

nanoparticles are smaller since they were exposed to air, prior to analysis. Ni and Co show a similar behavior. Qualitative statistical information for TiN/Fe system is presented in Figs. 1(g) and 1(h). Figure 1(g) shows histograms of nanoparticle size; Fig. 1(h) shows that nanotube diameter is correlated to nanoparticle size. The difference between nanotube diameter and nanoparticle size is related to the oxidation of the catalyst. As previously mentioned, the actual size of the particles during nanotube growth is smaller than the one estimated by *ex situ* characterization.

Nanoparticle formation is a critical step in surface-growth CNT CVD.¹³ This proves also for our TiN support

and Fe films, 1 nm or thinner, since only PP nanoparticles yield nanotube forests. CNT forests grow out of catalytic systems (such as Al_2O_3 -Fe) which hold CSIs that inhibit surface/bulk diffusion of catalyst nanoparticles on/into the support.¹⁵ This results in a narrow nanoparticle size distribution which leads to higher nanotube nucleation density and vertical alignment; because of the limited catalyst mobility, CNTs grow by root growth. We confirmed root growth in PP films by using interrupted growth conditions (Fig. 2). After PP, C_2H_2 flow was on for 1 min, stopped for 5 min, and then on for another 10 min. The growth of a two-layer mat with a thicker bottom layer confirmed base growth [Fig. 2(a)]. The

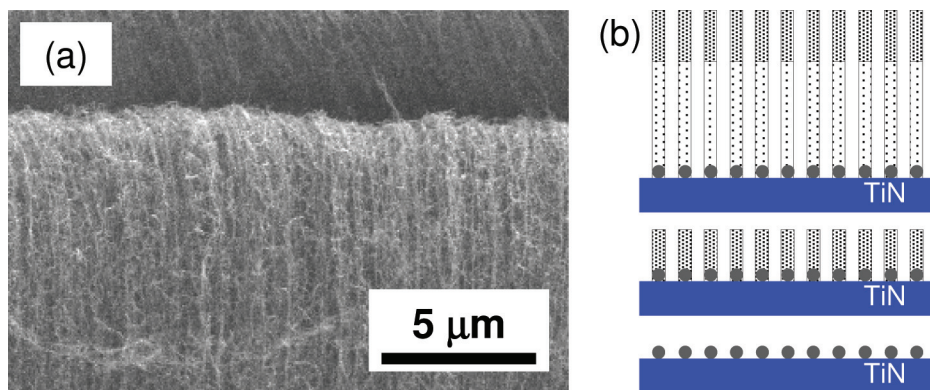


FIG. 2. (Color online) Root growth on PP samples. Cross-section SEM image of CNTs grown in 0.5 mbar of C_2H_2 at $600^\circ C$ on 1 nm Fe previously subject to PP. C_2H_2 was supplied for 1 min, stopped for 5 min, and restarted for another 5 min. (b) is a schematic cartoon of root growth processes for PP on TiN films.

thin top layer grew first (1 min growth), followed by the thicker bottom layer (10 min growth). Root growth on TiN is schematically represented on Fig. 2(b).

Based on these results, we suggest that PP promotes catalyst-support interactions that stabilize smaller catalyst nanoparticles. For the Al_2O_3-Fe system, it was easily shown, by *in situ* XPS that the interaction limiting Fe surface mobility is related to a Fe^{2+} and Fe^{3+} interface states.¹⁵ However, for PP samples, the interface state has proved much more difficult to assess. Firstly, due to the lack of characterization facilities capable of combining PP and *in situ* XPS/XRD; second, because upon air exposure (for *ex situ* characterization), PP samples undergo oxidation, and thus nanoparticles and their support interface change the chemical composition. Nevertheless, by combining *in situ* and *ex situ* XPS/XRD characterization at different stages of pretreatment/growth, we gain insight into PP and validate our hypothesis that PP stabilizes TiN-supported nanoparticles. We thoroughly study the stability of TiN, the interactions between TiN and Fe, and the stability of PP Fe nanoparticles.

A. TiN stability

The properties of TiN films strongly depend on the deposition techniques and the used parameters.²⁷ For this reason, we first examined how PP and CNT CVD impact on the thermal stability and surface roughness of our dc magnetron sputtered TiN. By AFM, we found that the roughness of bare TiN surface reduces during processing. As-deposited, TiN presents an RMS roughness of ~ 1.0 nm, which reduces to ~ 0.5 nm after 5 min PP (at $600^\circ C$ in 100 mbar of H_2 and dc plasma power of 50 W) and remains almost constant after 10 min CNT CVD in 0.5 mbar of C_2H_2 at same temperature and no plasma (not shown here). Therefore, the morphological changes observed on metal-coated TiN after PP [Figs. 1(d)–1(f)] are related to metal catalyst restructuring. To understand the roughness change, we performed *ex situ* XRD. A smoother surface morphology could arise from structural changes of TiN. However, XRD reveals no crystallographic modifications throughout the processing steps [Fig. 3(a)]. The main reflections due to cubic TiN do not change position or intensity on bare samples or coated with 1 nm Fe; nor are additional crystalline phases detected. So the changes of TiN

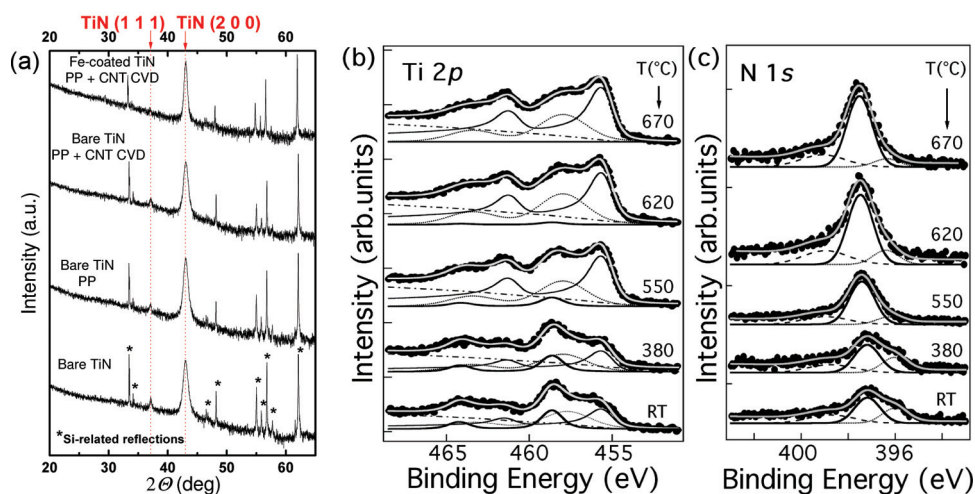


FIG. 3. (Color online) TiN stability during PP. (a) XRD spectra (logarithmic scale) of bare TiN, bare TiN after PP for 5 min at $600^\circ C$ in 100 mbar of H_2 and dc plasma power of 50 W, bare TiN after identical PP followed by CVD conditions (10 min in 0.5 mbar of C_2H_2 at same temperature), and Fe-coated TiN after same PP and CNT CVD. (b) and (c) are temperature-resolved XPS Ti $2p$ and N $1s$ core level lines of bare TiN upon vacuum heating. The black circles correspond to experimental data, while the gray line to fit results. The Ti $2p$ levels are reproduced using a Shirley background (dotted line) and 3 doublets, corresponding to Ti-N (thin continuous line), Ti^{4+} (thick line) and an intermediate state (dots) including Ti $2p$ shake up losses and Ti sub-oxides. The N $1s$ photoemission spectra are reproduced using a Shirley background (not shown) and 3 Gaussian components, corresponding to N-Ti (thick continuous line), N in interstitial sites (dotted line) and N in TiN_xO_y (dots).

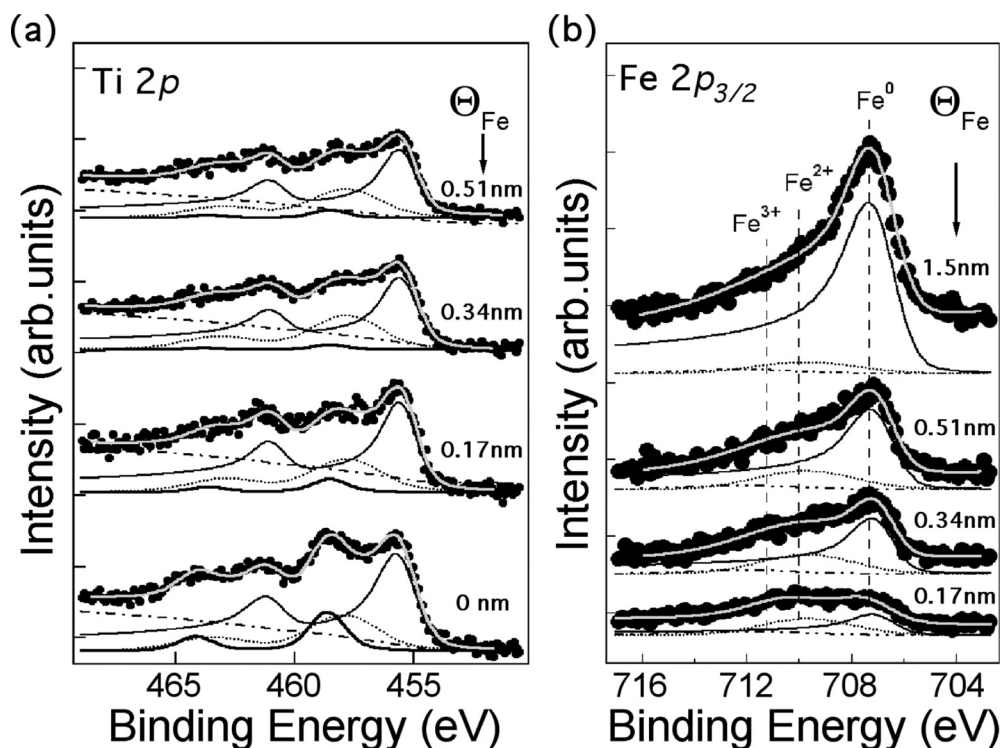


FIG. 4. Fe-TiN interactions. (a) and (b) are respectively XPS Ti 2p, Fe 2p_{3/2} core level lines of TiN subject to *in situ* RT Fe deposition at a constant deposition rate of $\sim 0.341 \text{ \AA min}^{-1}$ and different Fe coverage. The black circles correspond to experimental data, while the gray line to fit results. The Ti 2p levels are reproduced using a Shirley background (dotted line) and 3 doublets, corresponding to Ti-N (thin continuous line), Ti⁴⁺ (thick line) and an intermediate state (dots) including Ti 2p shake up losses and Ti sub-oxides. The Fe 2p_{3/2} spectra are reproduced using a Shirley background (not shown) and 3 Gaussian components, corresponding to metallic Fe⁰ (thin line), Fe²⁺ (dots) and Fe³⁺ (dotted line, negligible within our experimental resolution). Note that Fe progressively reduces Ti⁴⁺ (present at the TiN surface after air exposure) and forms Fe²⁺ at the interface. Ti⁴⁺ intensity is negligible for Fe coverage higher than 0.51 nm.

roughness can only be attributed to processing temperature. Increases of temperature give rise to mobility of surface atoms, which causes ordering of the structure by release of compressive residual stress that films develop after deposition.²⁸ This process is often enhanced by desorption of surface contaminants and/or reduction of surface oxides.

To assess surface processes, we performed *in situ* XPS after annealing of bare TiN. We observed that annealing at temperatures $>450 \text{ }^\circ\text{C}$ causes desorption of contaminants (such as H₂O or CO) and a progressive reduction of TiO_x and TiO_xN_y present at the surface (due to air exposure). Accordingly, as-reduced Ti reacts with atomic N forming TiN. This is shown in the temperature-resolved XPS spectra of Ti 2p and N 1s [Figs. 3(b) and 3(c), respectively]. It has been reported that the Ti 2p spectra shows shake-up peaks whose BE falls into the BE range of TiO_xN_y components.^{29,30} We note this often hinders the interpretation of TiO_xN_y chemistry, as it is based on the chemical shifts of BE of the Ti 2p spectra. So as to avoid misinterpretations, we reproduced the Ti 2p line shape by using only three components [Fig. 3(b)]: one for TiN ($\sim 455.5 \text{ eV}$, continuous line), one for fully oxidized Ti (Ti⁴⁺, $\sim 458.6 \text{ eV}$ disordered TiO₂, continuous thick line), and another for intermediate components (Ti shake-up, TiO_{x<2}, and TiO_xN_y, $\sim 458.0 \text{ eV}$ dotted line). No significant changes occur up to temperatures of $\sim 350 \text{ }^\circ\text{C}$. However, at $T > 380 \text{ }^\circ\text{C}$ the Ti 2p spectrum changes line shape, showing an increase in the TiN component and a decrease in the Ti⁴⁺ component. At the same time, the N 1s shows only the TiN component (at $\sim 397.5 \text{ eV}$, continuous line, Fig. 3c), whereas both the TiO_xN_y component (at $\sim 396 \text{ eV}$) and the interstitial N component (at $\sim 399 \text{ eV}$) disappear [dots and dotted lines in Fig. 3(c), respectively].³¹ The O 1s line shape also shows a loss of its intensity at about 532 eV, associated to reduction of N

oxides (not shown here). These patterns became more evident at temperatures higher than $550 \text{ }^\circ\text{C}$. At $670 \text{ }^\circ\text{C}$, the Ti⁴⁺ is completely reduced and the Ti 2p line shape is similar to that of stoichiometric TiN films, indicating that the intermediate component is mainly due to Ti 2p shake up.³² This implies that only a thin TiO_xN_y film remain on the surface, explaining thus the improvement in surface smoothness. We also note that the surface oxides desorption enhances the metallic state of the TiN surface. Photoemission valence bands measurements acquired using He I radiation ($h\nu = 21.2 \text{ eV}$), before and after annealing, show the appearance of the Fermi level after oxide desorption (not shown here). Importantly, the fact that TiN remains unchanged (during all processing steps) and/or improves its electrical conductivity satisfies a precondition for nanotube integration and justifies the investigation as potential conductive material support.

B. Fe-TiN interactions

PP and CNT CVD leave intact the surface morphology and crystalline structure of bare TiN. However, if coated with a metal and exposed to typical processing conditions, TiN strongly interact, physically and/or chemically, with the metal on top, and, unless a barrier is deposited in between, either interaction leads to partial/total catalyst deactivation. We assessed TiN-Fe interactions by performing *in situ* XPS before and after *in situ* Fe deposition (Fig. 4). We first found that, for low Fe coverage ($<1 \text{ nm}$) and low deposition rate, Fe starts diffusing into TiN immediately after deposition, even at RT. We concluded this after RT depositing Fe for 60 min, at same deposition rates, on TiN and Al₂O₃ as reference support. By using XPS core levels attenuation and Fe absolute intensity, we found the thickness of Fe onto TiN was 1.64 nm, while onto Al₂O₃ (where no or negligible Fe inter-

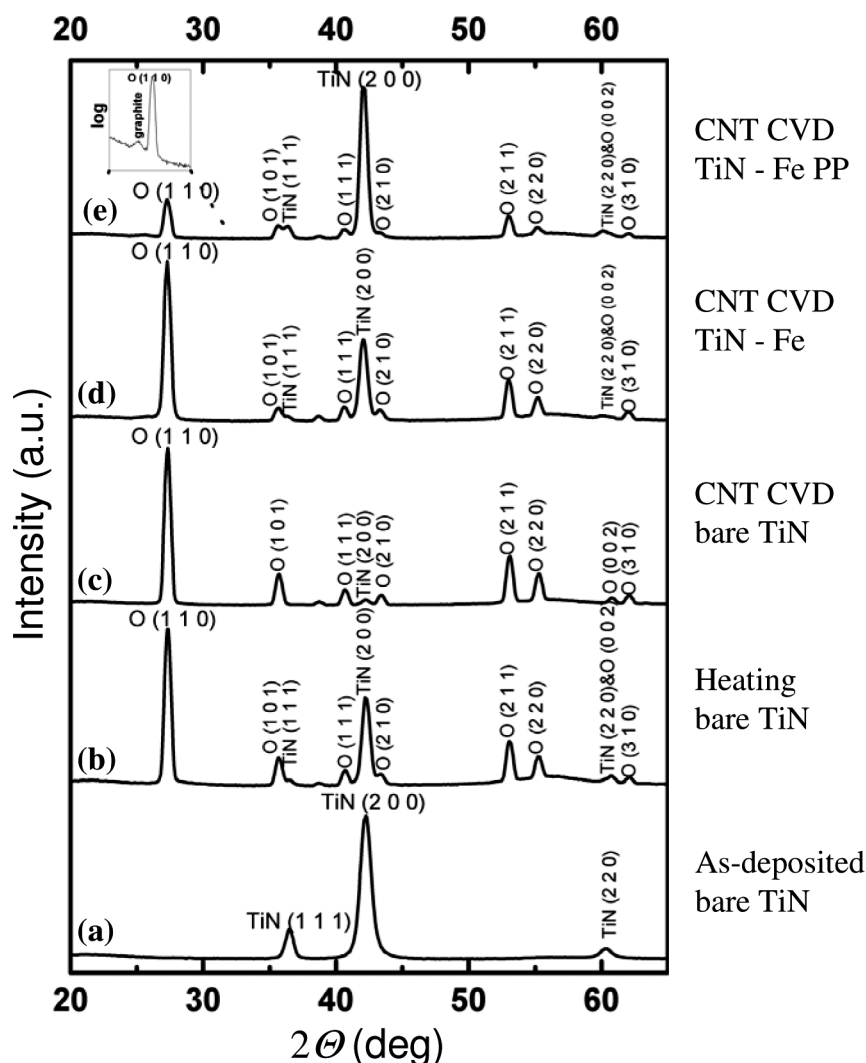


FIG. 5. Stability of TiN/Fe nanoparticles. XRD spectra of (a) bare TiN at RT, (b) bare TiN upon heating up to a temperature of 650 °C in 200 mbar of Ar:H₂ (30:10 sccm) for 30 min, (c) bare TiN upon heating at same conditions followed by 30 min of same conditions plus 1 sccm of C₂H₂, (d) TiN coated with 4 nm Fe at same conditions as (c), and (e) TiN coated with 4 nm Fe previously subject to PP/air exposure and same processing as (c).

diffusion takes place at RT) was 2.05 nm. It is known that Fe diffusion into TiN depends on the TiN morphology/surface defects and is strongly enhanced by temperature. For our TiN, annealing in vacuum at 550 °C for 5 min causes a decrease of ~55% of the Fe 2*p* signal of a 3.5 nm Fe film RT deposited (not shown here).

We also found several reactions taking place at the TiN/Fe interface. Fe reduces Ti⁴⁺ oxides (present at the TiN surface) and forms Fe oxides at its interface [Figs. 4(a) and 4(b)]. This can be seen on both the Ti⁴⁺ component (on the Ti 2*p* core level) and on the Fe²⁺ component (on the Fe 2*p*_{3/2} core level), which, respectively decreases and increases their intensities, as function of Fe coverage [Figs. 4(a) and 4(b), respectively]. A similar observation has been reported by depositing Fe films on single crystal TiO₂.³³ Our data confirm that the deposition of 0.5 nm of Fe is sufficient to reduce all Ti⁴⁺ and transform the TiN-Fe interface into a Fe²⁺ state [Fig. 4(b)]. Either Fe inter-diffusion into TiN or Fe reaction with Ti oxides deactivates the Fe.³⁴

The growth results [Figs. 1(a)–1(c)] indicate, however, that PP prevents (at least partially) such deactivating interactions, but somewhat stabilizes the Fe catalyst. We further studied the stability of PP nanoparticles by *in situ* XRD at

different processing steps (Fig. 5). We evaluated un-pretreated and previously plasma-pretreated TiN coated with 4 nm Fe; for reference, we used bare TiN. We found that PP stabilizes TiN against material interactions and that PP nanoparticles remain catalytically active for nanotube nucleation, even after air exposure, revealing thus a strong catalyst-support stability after PP. As-deposited bare TiN presents the typical reflections of (111), (200), and (220) TiN [Fig. 5(a)]. Upon heating (in our oxygen-containing Ar:H₂), it undergoes oxidation, as revealed by the appearance of several reflections attributed to TiO₂, [Fig. 5(b)]. This is typical in metallic films exposed to low-pressure, oxidising environments.³⁵ Finally, upon C₂H₂ exposure, a further reduction of the TiN (200) and TiN (111) reflections is observed [Fig. 5(c)], implying oxidation continues during CNT CVD. No graphite reflections are identified, consistent with the absence of Fe catalyst.

The appearance of TiO₂ reflections reflects how strongly TiN tends to interact with reactive atmospheres (note that the CVD system for *in situ* XRD is not the same as used for PP). This compares to TiN coated with 4 nm Fe. As-loaded, the sample shows the same reflections as bare TiN and during heating also transforms into TiO₂ (not shown here). Upon

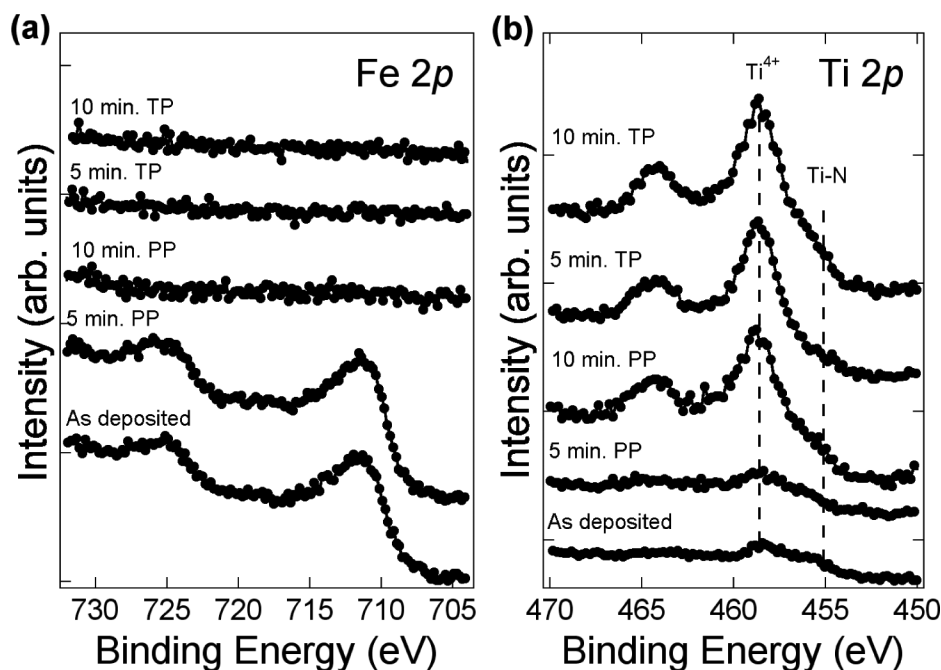


FIG. 6. Stability of PP nanoparticles. (a) and (b) are respectively XPS Ti $2p$ and Fe $2p$ core level lines of TiN coated with 1 nm Fe, as such, or subject to PP or TP. PP was performed at 600 °C in 100 mbar of H_2 and dc plasma power of 50 W for 5, 10, and 15 min, while TP was performed at exactly same conditions except for plasma off.

C_2H_2 exposure, a reflection associated to graphite appears, but results almost undistinguishable in the scan due to its very low intensity [Fig. 5(d)]. The TiN (200) and TiN (111) reflections retain much of their intensities, in comparison to same process on bare TiN [Fig. 5(c)].

In contrast, the 4-nm-Fe-coated TiN sample, previously plasma pretreated and exposed to air is much less oxidized into TiO_2 . We found that upon heating all TiN intensities remain almost invariable (not shown here). As a semi-quantitative expression for the degree of phase changes, we compare the ratios between the highest intensities of TiO_2 reflections to those of TiN. The ratio decreases from ~ 50 (for bare TiN) to ~ 1.7 (for Fe-coated TiN), to finally reach ~ 0.2 for the PP sample. During CNT CVD, the intensity of the graphite reflection is much more intense [Fig. 5(e) and inset at logarithmic scale]. By SEM we confirm the presence of nanotubes (not shown here). These results demonstrate that PP stabilizes the TiN support and that PP nanoparticles certainly remain stable/catalytically active, even after air exposure.

C. Stability of PP nanoparticles

The fact that PP nanoparticles remain catalytically active (even after air exposure) led us to another route for investigating their surface stability. Surface stability of nanoparticles can be examined by exposing supported nanoparticles to identical annealing conditions and increasing annealing times.²⁵ Stable nanoparticles show little changes in their dimensions/composition as annealing time elapses, while nonimmobilized nanoparticles diffuse on the surface or bulk of the support, changing their topology and chemical patterns. *Ex situ* XPS allowed us to follow the catalyst evolution at different TP or PP times (Fig. 6). For this, we performed TP or PP (at 50 W dc plasma) on TiN coated with 1 nm Fe at 650 °C in 100 mbar of H_2 for 5, 10, and 15 min and

then performed *ex situ* XPS. We found that Fe signal is present after Fe deposition and remains almost invariable on the 5-min PP sample, but completely disappears on the 5-min TP sample [Fig. 6(a)]. We also observed that annealing times longer than 5 min lead to complete loss of Fe signal, regardless of the type of pretreatment. As Fe signal disappears, a strong TiO_2 signal is observed on the Ti $2p$ core level spectrum [Fig. 6(b)]. Oxidation takes place as TiN results uncovered due to Fe inter-diffusion. These transformations are also reflected in the N $1s$ and O $1s$ core level spectra (not shown here). The changes in lineshapes are attributed to N and Ti oxides.

We interpret the fact that the Fe signal is still present on the 5-min PP sample as a confirmation that PP nanoparticles resist bulk diffusion for longer times than those obtained by TP, due to higher support stability, as previously observed by *in situ* XRD [Fig. 5(e)]. In contrast, the loss of Fe signal, observed during TP or any long pretreatment, is due to Fe nanoparticle diffusion into the TiN support, consistent with the strong TiN-Fe interactions previously observed by *in situ* XPS during deposition/annealing [Figs. 4(a) and 4(b)]. This result stresses that the effect of plasma on support-nanoparticle stability is overcome as PP exceeds a certain critical time, moment in which nanoparticles start diffusing into the underlying TiN (Fig. 7). For our TiN/1 nm Fe catalyst system, under the described PP conditions, the PP critical time is found to be around 5 min. Very short (3 min or less) or much longer PP (e.g., 10 min) annealing times yield sparse or not growth at all, as samples receiving TP do.

D. Nanotube growth on PP nanoparticles

We find that PP enhances nanotube growth on many catalyst systems, including SiO_2 -Ni, Ta-Fe, and TiN-Ni/-Co/-Fe, which suggests a generic mechanism.^{23,24,36} One of the advantages of PP is that, regardless of the system, it favors

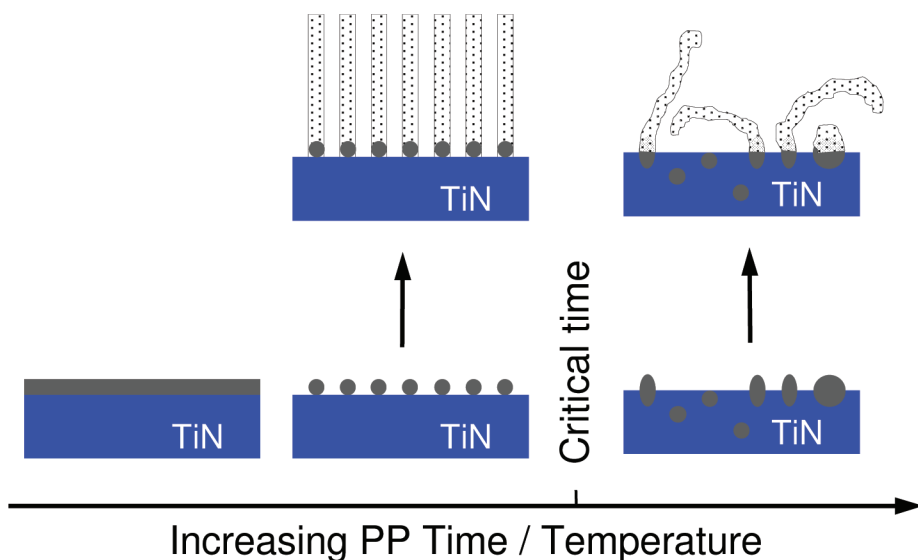


FIG. 7. (Color online) Growth model for PP nanoparticles. Schematic diagram of PP sequence (of Fe-coated TiN) as function of time or temperature. At PP critical time nanoparticles start diffusing into the underlying support. Uncontrolled growth after PP critical time is similar to TP growth.

metal restructuring into smaller domains than TP, which results into more active catalytic nanoparticles. Here we argue that the superior catalytic activity of PP nanoparticles is, to a great extent, related to topographical effects, as experiments and characterization prove a striking correlation between catalyst-support stability and growth results. This is schematically represented in Fig. 7.

We propose that during PP (at empirically optimized conditions) metal films restructure into small nanoparticles, which, upon the effect of plasma, do not immediately surface/bulk diffuse (Fig. 7). The delay of diffusion/nanoparticle stabilization, however, degrades with pretreatment time. If no further changes are introduced into the system, before reaching a certain critical time, PP nanoparticles will completely diffuse and lose their catalytic activity. For Fe, the loss of catalytic activity is due to bulk diffusion into TiN [Fig. 5(a)]. Conversely, if the carbon source is introduced before the PP critical time, PP nanoparticles decompose the carbon source and nucleate nanotubes before diffusing into TiN. Only if nucleation occurs well before complete diffusion, equilibrium is reached. Nanoparticles remain then anchored to the substrate and nanotubes continue to grow by root growth (Fig. 2). The homogeneity of catalyst size and the kinetics of carbon source decomposition/carbon segregation are determinant factors for reaching this equilibrium.

We speculate that hydrogen plasma could have an additional, positive kinetic effect.³⁷ H ions could chemisorb on the catalyst surface and significantly modify its properties (e.g., surface energy), altering the interaction with the carbon source. This could accelerate the adsorption of the carbon source to the catalyst surface and/or give higher carbon diffusivities during nanotube nucleation.³⁸ More characterization is still necessary to assess chemical process at the surface of PP nanoparticles as well as at their interface with the support.

On the other hand, by following the traditional TP, metal nanoparticles (formed by annealing films of ~ 1 nm or thinner) immediately diffuse into the underlying TiN substrate, as the temperature or time increase. Due to the sud-

deness of diffusion, there not exists a TP critical time. Therefore, the catalytic activity of the nanoparticles is reduced to the extent that poor or no growth occurs, even for very short TP times. We note that TP growth results are similar to those after PP critical time (Fig. 7), hence validating our hypothesis that PP stabilizes/immobilizes catalytic nanoparticles. The TiN-Fe interactions depend on the properties of the TiN film, so the TP critical time could vary with the type of film utilized. We are now evaluating nanotube growth on TiN films deposited by different techniques or conditions and catalyst films thicker than 1 nm.

E. Electrical characterization

We finally performed electrical characterization on TiN-supported nanotube forests and (for comparison) on bare TiN as deposited and after processing steps (Fig. 8). Bare TiN after deposition or after PP/CNT CVD presents very similar I-V relationships [Fig. 8(a)], consistent with the observed stability of TiN crystallographic phases after processing [Fig. 3(a)]. We measured an electrical resistance of $37.5 \pm 3.8 \Omega$ for bare TiN, which remains practically unchanged throughout processing steps: $37.4 \pm 4.1 \Omega$ after PP and $34.6 \pm 3.5 \Omega$ after CNT CVD. These figures are higher than expected for TiN and attributed to oxidation of its surface (upon air exposure). The formation of resistive TiO_2/TiON layers is largely detrimental for electrical conduction.

When the electrical evaluation is performed through the nanotube forests, the overall resistance increases from $\sim 35 \Omega$ to $> 1.2 \text{ k}\Omega$ [Figs. 8(b) and 8(c)]. The I-V response proves the conduction through the nanotube forests and, again, the stability of TiN after PP/PP CNT CVD. The overall contact resistance, 2 orders of magnitude higher than bare TiN, could derive from a poor contact between nanotube forest and TiN support, i.e., a high $R_{\text{Forest-TiN}}$ [Fig. 8(b)]. With the present setup (direct contact of the forest with the probe tip), we cannot estimate its contribution, but only assess the overall

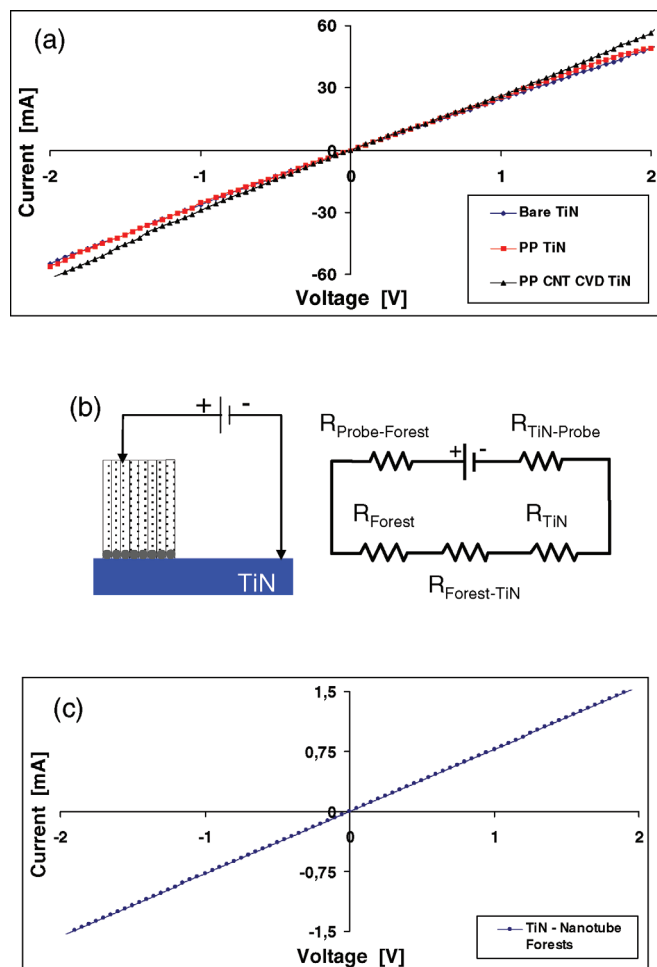


FIG. 8. (Color online) Electrical evaluation of nanotube forests on TiN. I-V curves of (a) bare TiN after processing and (c) after growth of nanotube forests. (b) Schematic diagram of equivalent circuit of the electrical characterization.

resistance is ohmic, which is essential for nanotube integration as interconnects.

The demonstration of growth of conductive nanotubes forests on TiN is an advance for the integration of CNTs into vias and interconnects. TiN remains stable after PP and nanotube forests present ohmic conduction. However, many of the integration requirements (like nanotube surface density or growth temperature) still need to be met. This will involve further technology development/optimization of PP and growth conditions. Work is in progress for this.^{39,40} We highlight that TiN can be patterned on horizontal/vertical surfaces (respectively by sputtering/atomic layer deposition); therefore, this material warrants further studies as support for nanotube growth. We are currently dealing with catalyst immobilization by using alternative PP to H plasma.

IV. CONCLUSIONS

Hydrogen plasma pretreatment is found to enhance the formation and stabilization of Fe nanoparticles onto the TiN substrate, despite strong TiN-Fe interactions, without affecting the crystallographic structure and conductivity of the support. This results into more static nanoparticles than those

obtained by thermal pretreatment followed by nucleation/growth of nanotube forests. However, the catalytic activity of plasma treated nanoparticles degrades with time, so that nucleation must be set before reaching a critical time, moment in which plasma treated nanoparticles start to diffuse into the underlying substrate. These nanotube forests are conductive and show ohmic behavior.

- ¹S. Fan, M. G. Chapline, N. R. Franklin, T. W. Tomblor, A. M. Cassell, and H. Dai, *Science* **283**, 512 (1999).
- ²M. Katagiri, N. Sakuma, M. Suzuki, T. Sakai, S. Sato, T. Hyakushima, M. Nihei, and Y. Awano, *Jpn. J. Appl. Phys.* **47**, 2024 (2008).
- ³M. Nihei, M. Horibe, A. Kawabata, and Y. Awano, *Jpn. J. Appl. Phys.* **43**, 1856 (2004).
- ⁴J. Robertson, G. Zhong, H. Telg, C. Thomsen, J. M. Warner, G. A. D. Briggs, U. Detlaff, and S. Roth, *Appl. Phys. Lett.* **93**, 163111 (2008).
- ⁵B. C. Bayer, S. Sanjabi, C. Baetz, C. T. Wirth, S. Esconjauregui, R. S. Weatherup, Z. H. Barber, S. Hofmann, and J. Robertson, "Carbon nanotube forest growth on NiTi shape memory alloy thin films for thermal actuation," *Thin Solid Films* (in press).
- ⁶P. Avouris and J. Chen, *Mater. Today* **9**, 46 (2006).
- ⁷K. Hata, D. N. Futaba, K. Mizuno, T. Namai, M. Yumura, and S. Iijima, *Science* **306**, 1362 (2004).
- ⁸Y. L. Li, I. A. Kinloch, and A. H. Windle, *Science* **304**, 276 (2004).
- ⁹X. Li, A. Cao, Y. J. Jung, R. Vijtai, and P. M. Ajayan, *Nano Lett.* **5**, 1997 (2005).
- ¹⁰M. Cantoro, S. Hofmann, S. Pisana, V. Scardaci, A. Parvez, C. Ducati, A. C. Ferrari, A. M. Blackburn, K. Y. Wang, and J. Robertson, *Nano Lett.* **6**, 1107 (2006).
- ¹¹A. R. Harutyunyan, G. A. Chen, T. M. Paronyan, E. M. Pigos, O. A. Kuznetsov, K. Hewaparakrama, S. M. Kim, D. Zakarov, E. A. Stach, and G. U. Sumanasekera, *Science* **326**, 116 (2009).
- ¹²J. Robertson, G. Zhong, S. Hofmann, B. C. Bayer, S. Esconjauregui, H. Telg, and C. Thomsen, *Diam. Rel. Mat.* **18**, 957 (2009).
- ¹³S. Hofmann, R. Sharma, C. Ducati, G. Du, C. Mattevi, C. Cepek, M. Cantoro, S. Pisana, A. Parvez, A.C. Ferrari, R. Dunin-Borkowski, S. Lizzit, L. Petaccia, A. Goldoni, and J. Robertson, *Nano Lett.* **7**, 602 (2007).
- ¹⁴S. Hofmann, R. Blume, C. T. Wirth, M. Cantoro, R. Sharma, C. Ducati, M. Havecker, S. Zafeiratos, P. Schnoerch, A. Oestereich, D. Teschner, M. Albrecht, A. Knop-Gericke, R. Schlogl, and J. Robertson, *J. Phys. Chem. C* **113**, 1648 (2009).
- ¹⁵C. Mattevi, C. T. Wirth, S. Hofmann, R. Blume, M. Cantoro, C. Ducati, C. Cepek, A. Knop-Gericke, S. Milne, C. Castellarin-Cudia, S. Dolafi, A. Goldoni, R. Schloegl, and J. Robertson, *J. Phys. Chem. C* **112**, 12207 (2008).
- ¹⁶M. Pinault, V. Pichot, H. Khodja, P. Launois, C. Reynaud, and M. Mayne-L'Hermitte, *Nano Lett.* **5**, 2394 (2005).
- ¹⁷T. Iwasaki, R. Morikane, T. Edura, M. Tokuda, K. Tsutsui, Y. Wada, and H. Kawarada, *Carbon* **45**, 2351 (2007).
- ¹⁸A. M. Rao, D. Jacques, R. C. Haddon, W. Zhu, C. Bower, and S. Jin, *Appl. Phys. Lett.* **76**, 3813 (2000).
- ¹⁹T. de los Arcos, F. Vonau, M. G. Garnier, V. Thommen, H.-G. Boyen, P. Oelhafen, M. Duggelin, D. Mathis, and R. Guggenheim, *Appl. Phys. Lett.* **80**, 2383 (2002).
- ²⁰Y. Wang, Z. Luo, B. Li, P. Ho, Z. Yao, L. Shi, E. N. Bryan, and R. J. Nemanich, *J. Appl. Phys.* **101**, 124310 (2007).
- ²¹D. Yokoyama, T. Iwasaki, T. Yoshida, H. Kawarada, S. Sato, T. Hyakushima, M. Nihei, and Y. Awano, *Appl. Phys. Lett.* **91**, 263101 (2007).
- ²²J. García-Céspedes, S. Thomasson, K. B. K. Teo, I. A. Kinloch, W. I. Milne, E. Pascual, and E. Bertran, *Carbon* **47**, 613 (2009).
- ²³S. Esconjauregui, B. C. Bayer, M. Fouquet, C. T. Wirth, C. Ducati, S. Hofmann, and J. Robertson, *Appl. Phys. Lett.* **95**, 173115 (2009).
- ²⁴B. C. Bayer, S. Hofmann, C. Castellarin-Cudia, R. Blume, C. Baetz, S. Esconjauregui, C. T. Wirth, R. A. Olivier, C. Ducati, A. Knop-Gericke, R. Schlögl, A. Goldoni, C. Cepek, S. Hofmann, and J. Robertson, *J. Phys. Chem. C* **115**, 4359 (2011).
- ²⁵C. Zhang, F. Yan, C. S. Allen, B. C. Bayer, B. J. Hickey, D. Cott, G. Zhong, and J. Robertson, *J. Appl. Phys.* **108**, 024311 (2010).
- ²⁶G. Zhong, T. Iwasaki, and H. Kawarada, *Carbon* **44**, 2009 (2006).
- ²⁷O. Knotek, M. Böhmer, and T. Leyendecker, *J. Vac. Sci. Technol. A* **4**, 2695 (1986).
- ²⁸F. Vaz, L. Rebouta, P. Goudeaub, T. Girardeaub, J. Pacaudb, J. P. Riviereb, and A. Traversec, *Surf. Coat. Tech.* **146-147**, 274 (2001).

- ²⁹B. J. Burrow, A. E. Morgan, and R. C. Ellwanger, *J. Vac. Sci. Technol. A* **4**, 2463 (1986).
- ³⁰N. C. Saha and H. G. Tompkins, *J. Appl. Phys.* **72**, 3072 (1992).
- ³¹I. Bertóti, M. Mohai, J. L. Sullivan, and S. O. Saied, *Appl. Surf. Sci.* **84**, 357 (1995).
- ³²M. Delfino, J. A. Fair, and D. Hodul, *J. Appl. Phys.* **71**, 6079 (1992).
- ³³H. Mostéfa-Sba, B. Domenichini, and S. Bourgeois, *Surf. Sci.* **437**, 107 (1999).
- ³⁴Q. Fua and T. Wagner, *Surf. Sci. Rep.* **62**, 431 (2007).
- ³⁵J. Park, Y. Ryu, H. Kim, and Y. Choongho, *Nanotechnology* **20**, 105608 (2009).
- ³⁶M. Cantoro, S. Hofmann, C. Mattevi, S. Pisana, A. Parzev, A. Fasoli, C. Ducati, V. Scardaci, A. C. Ferrari, and J. Robertson, *J. Appl. Phys.* **105**, 064304 (2009).
- ³⁷W. F. Egelhoff and D. A. Steigerwald, *J. Vac. Sci. Technol. A* **7**, 2167 (1989).
- ³⁸Z. Paal and P. G. Menon, *Hydrogen Effects in Catalysis* (Dekker, New York, 1988).
- ³⁹S. Esconjauregui, M. Fouquet, B. C. Bayer, C. Ducati, R. Smajda, S. Hofmann, and J. Robertson, *ACS Nano* **4**, 7431 (2010).
- ⁴⁰S. Esconjauregui, M. Fouquet, B. C. Bayer, S. Eslava, S. Khachadorian, S. Hofmann, and J. Robertson, *J. Appl. Phys.* **109**, 044303 (2011).